

# Three-dimensional convective dissolution of carbon dioxide into brine

**Paul Fruton**

Université de Pau et des Pays de l'Adour <https://orcid.org/0000-0003-3826-4178>

**Aziza Nauruzbaeva**

Université de Pau et des Pays de l'Adour

**Henri Bataller**

Université de Pau et des Pays de l'Adour <https://orcid.org/0000-0002-4028-0700>

**Cédric Giraudet**

Université de Pau et des Pays de l'Adour

**Alberto Vailati**

Università degli Studi di Milano <https://orcid.org/0000-0002-3119-6021>

**Fabrizio Croccolo** (✉ [fabrizio.croccolo@univ-pau.fr](mailto:fabrizio.croccolo@univ-pau.fr))

Université de Pau et des Pays de l'Adour <https://orcid.org/0000-0001-6832-400X>

---

## Article

### Keywords:

**Posted Date:** January 7th, 2022

**DOI:** <https://doi.org/10.21203/rs.3.rs-1200143/v1>

**License:**   This work is licensed under a Creative Commons Attribution 4.0 International License.

[Read Full License](#)

---

# Three-dimensional convective dissolution of carbon dioxide into brine

Paul Fruton<sup>1</sup>, Aziza Nauruzbaeva<sup>1</sup>, Henri Bataller<sup>1</sup>, Cédric Giraudet<sup>1</sup>, Alberto Vailati<sup>2</sup>, and Fabrizio Croccolo<sup>1,\*</sup>

<sup>1</sup>Universite de Pau et des Pays de l'Adour, E2S UPPA, CNRS, TotalEnergies, LFCR UMR5150, Anglet (France)

<sup>2</sup>Dipartimento di Fisica "Aldo Pontremoli", Università degli Studi di Milano, Milano (Italy)

\*fabrizio.croccolo@univ-pau.fr

## ABSTRACT

The sequestration of carbon dioxide (CO<sub>2</sub>) through storage into deep saline aquifers represents an indispensable support technology to achieve the zero-carbon target necessary to mitigate the impact of CO<sub>2</sub> on climate change. The effectiveness of the sequestration process, partly driven by the convective dissolution of CO<sub>2</sub> in brine, is nowadays well characterized for two-dimensional geometries, low permeabilities, and small pressures of injection of CO<sub>2</sub>. However, reliable predictions of process-efficiency are missing because of the lack of full understanding of the three-dimensional (3D) spatio-temporal behaviour of CO<sub>2</sub>-rich convective fingers in brine over a large range of injection pressures. Here, we show that the convective dissolution is determined by the instability of the boundary layer formed at the interface between the two phases and is totally independent of the overall vertical size. Experiments were conducted over a broad range of injection pressures, close to process-relevant conditions. The results show the formation of complex 3D structures, including interconnecting stream tubes at the CO<sub>2</sub>-liquid interface, which could not be detected in previous 2D Hele-Shaw studies, and fingerings. A scale-free theoretical modelling of the convective process allows us to remap our laboratory results to length-scales of relevance for geological reservoirs. The experiments and the model show that the times needed for the onset of convection and the convective flux are independent of the system size.

Over the latest decades, the concentration of carbon dioxide (CO<sub>2</sub>) in the atmosphere has increased dramatically, leading to a worldwide noticeable change on the climate<sup>1-3</sup>. Predictions foresee that the increase in average Earth surface temperature will keep rising. Attempts are therefore being made to reduce CO<sub>2</sub> emissions by, e.g., converting it into valuable products<sup>4,5</sup> or safely storing it<sup>6,7</sup>. The mitigation solution of relevance for the present work consists in sequestering CO<sub>2</sub> in deep saline aquifers by injecting it at supercritical state inside geological reservoirs<sup>8</sup>. A critical issue that could limit the effectiveness of this approach is the large amount of time needed for dissolving CO<sub>2</sub> into brine with respect to the required flow rate. These timescales can be significantly reduced taking advantage of convection that arises in the presence of a sufficiently large unstable density stratification<sup>9,10</sup>. For instance, it has been shown that the convective mass flux is of about one order of magnitude larger than the diffusive one during the convective dissolution of CO<sub>2</sub> into brine<sup>11</sup>. While the impact of brine composition<sup>11-14</sup> and porous medium permeability<sup>15-17</sup> on the onset time of convection was investigated, most of these studies were conducted at low pressures and in a Hele-Shaw geometry<sup>14,18-25</sup>. Owing to the small width over length aspect ratio of Hele-Shaw cells, the results are restricted to the Rayleigh-Darcy regime<sup>26</sup>. Since the presence of large-scale high-permeability volumes, e.g., cracks and fractures, enhances the mass transfer of CO<sub>2</sub> in saline aquifers<sup>27</sup>, experimental results on the spatio-temporal evolution of convective patterns in a fully 3D-configuration in the Rayleigh-Taylor regime are desirable.

The model system employed to investigate the convective dissolution process is represented by a horizontal layer of brine overlaid with CO<sub>2</sub> whose pressure is controlled. While CO<sub>2</sub> dissolves into brine, an interfacial liquid layer, with a density larger than that of the underlying brine, grows diffusively in the bulk<sup>28</sup>. When the density difference and the layer thickness are sufficiently large, a solutal convective instability, in the form of plumes, takes place<sup>9</sup>. We show that the onset time of convection and the dissolution rate are entirely dominated by the critical thickness of the boundary layer. Similar findings were observed for turbulent Rayleigh-Bénard convection<sup>29-32</sup>. The definition of dimensionless parameters allows to achieve a scale-free description suitable to upscale results from laboratory experiments to the much larger geological length scales of relevance for CO<sub>2</sub> storage in saline aquifers.

## Experimental system

Experiments were conducted in a 5 mm thick and 20 mm large cylindrical high-pressure cell. At the beginning, a 2 mm thick liquid layer, pre-saturated with CO<sub>2</sub> at atmospheric pressure is injected into the cell. Thereafter, CO<sub>2</sub> is rapidly injected on top of it at various pressures with the help of a high-pressure pump; see Methods. The complete circuit, including the pump, is maintained at a constant temperature of (308.2±0.5) K. The liquid consists of degassed water with 0, 1, or 3 mol·kg<sup>-1</sup> of sodium chloride (NaCl). The pressure difference applied to the system ranges from 0.34 to 6 MPa. Further experiments were conducted at pressure differences up to 10 MPa, where CO<sub>2</sub> is in supercritical state, but the strength of the turbulent flow in the CO<sub>2</sub> layer and the phase-change hinder the determination of the onset time of convection. Since the amount of CO<sub>2</sub> dissolved in brine does not vary much between 6 and 10 MPa<sup>33</sup> at this temperature, the present results are directly transferable to process engineering conditions.

The formation and dissipation of convective patterns are visualized by the shadowgraph optical projection method (see Methods), routinely employed in our laboratories for investigating non-equilibrium refractive index fluctuations<sup>34,35</sup> and convective instabilities<sup>36,37</sup>. During the dissolution process, we grab continuously shadowgraph images until macroscopic thermodynamic equilibrium is reached. We mainly investigated the growth and relaxation of patterns in the direction parallel to the gravity field. To provide a more comprehensive view on the pattern behaviour, some additional experiments were conducted with the setup tilted by 90°. In this configuration, the spreading of plumes is observed in the direction perpendicular to the gravity field.

## Results

### 3D spatio-temporal behaviour of the convective dissolution process.

At the beginning of each experimental run, the increase of the pressure of CO<sub>2</sub> determines a transient diffusion process that eventually leads to convection. The left part of Fig. 1 shows typical shadowgraph images acquired when the pressure is increased from 0.1 to 2.1 MPa for pure water. The corresponding movie can be found in the supplementary material. When CO<sub>2</sub> reaches the gas-liquid interface, the variance of each image difference provides a quantitative estimation of the mean squared amplitude of perturbations of the optical light path determined by the formation of convective structures. The variance, as shown in the right part of Fig. 1, represents a simple and reliable integrated information for understanding the development of a convective instability inside the sample<sup>37</sup>. Each of the image differences consists in the subtraction between an image acquired at a given time and a reference image. The time evolution of the image difference variance allows to clearly identify eight different phases denoted by **(a)-(h)**, themselves grouped in two main categories: the growth (I) and the relaxation (II) of patterns.

**I. Growth of convective patterns.** After a short initial phase where the injection of CO<sub>2</sub> determines transient disturbances in the vapor phase **(a)**, the contrast of image differences remains small and constant until a latency time  $t_c$  **(b)**. This featureless stage corresponds to the diffusive growth of a CO<sub>2</sub>-rich liquid boundary-layer formed at the vapor-liquid interface<sup>27</sup>. The diffusive growth ends at the onset time of convection  $t_c$ , when the thickness of the boundary-layer is sufficiently large to trigger buoyancy-driven instabilities for a given density difference. Since the time needed for the Fick diffusion process to evolve across the complete liquid layer thickness  $t_D = h^2/\pi D$  is much larger than  $t_c$ , advection dominates over diffusion immediately after  $t_c$ . This determines a sharp increase in the contrast and the appearance of patterns **(c)**. For all experimental runs, the convective pattern is firstly characterized by the presence of some horizontal stream tubes at the liquid-liquid interface. Gradually, some viscous plumes propagating vertically into the bulk appear along the stream tubes **(d)**.

The maximum optical contrast **(e)** is reached at time  $t_m$  and is several orders of magnitude larger than the one at the start of the convective process  $t_c$ . Here, further horizontal stream tubes have emerged in the entire bulk and, again, downward viscous plumes appear along them. As it will be discussed later, both  $t_c$  and  $t_m$  are independent of the liquid layer thickness. Thus, at  $t_m$ , the mixing inside the bulk has just started, and the dissolution rate is maximum. Furthermore, we observe the emergence of a Voronoï-like structure around the center of each lattice. It is associated with plumes reaching the bottom of the cell. They occur shortly before  $t_m$  in the case of pure water. In brine, they were observed after  $t_m$  due to its larger viscosity.

**II. Relaxation of convective patterns.** The rapid growth of patterns is followed by a relaxation process. The first exponential step of relaxation determines a decrease of the contrast in a time  $t_r$  to an almost constant value, corresponding to a stable regime where the convective flux can be assumed constant and the flow of CO<sub>2</sub> takes place mostly in columns crossing the bulk from the liquid-liquid interface to the cell bottom **(f)**. The origin of this decrease is twofold. First, we notice that the horizontal stream tubes start to split in plumes. Even though there are stream tubes still remaining and new isolated plumes emerging, this process leads to the creation of pattern-free areas that represent a larger proportion than at  $t_m$ . Furthermore, at that moment, the first patterns already reached the bottom of the cell, and the mixing inside the bulk has started. The density difference between the boundary layer and the bulk has decreased, which explains that the patterns are less contrasted than at  $t_m$ . After the constant flux regime, a second relaxation takes place until the shut-down of the convective regime  $t_{sd}$ . Convection

cannot be sustained any more since the  $\text{CO}_2$  dissolved into water has almost reached its saturation concentration in the bulk (g). Here, the remaining patterns are dissipating diffusively in the bulk and, after some time, the contrast reaches its initial value (h) where the system is at macroscopic thermodynamic equilibrium. As reflected by the small jumps in the contrast, the relaxation process exhibits intermittency, determined by the random emergence of plumes. The 3D spatio-temporal evolution of growth and dissipation of convective patterns was found qualitatively similar for both water and brine, independent of the salt concentration and the pressures of injection.

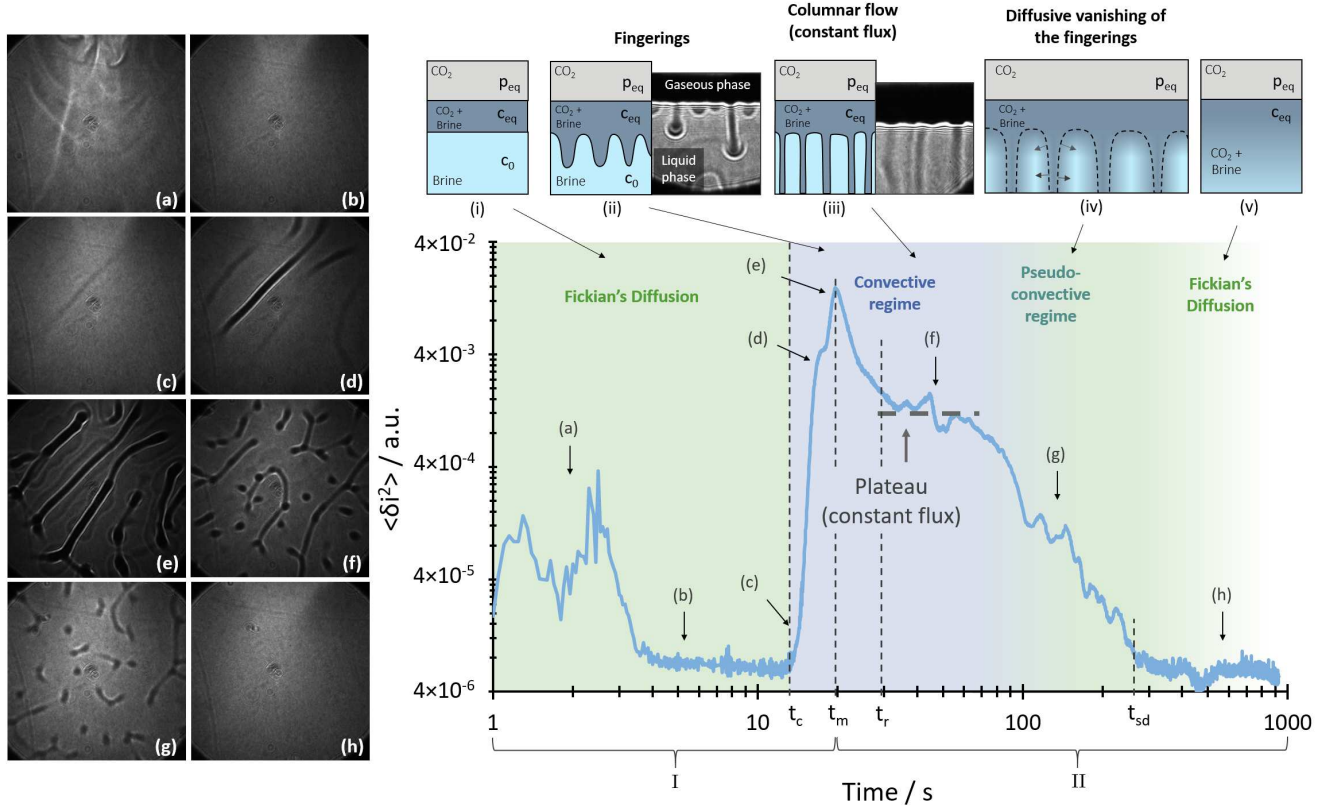


**Figure 1. 3D spatio-temporal evolution of the convective dissolution process** for  $\text{CO}_2$  dissolved in pure water when the pressure increases from 0.1 to 2.1 MPa. **Left:** Shadowgraph images taken at times representative of the different processes occurring while  $\text{CO}_2$  dissolves in brine or pure water. **Right:** Time evolution of the variance  $\langle \delta i^2 \rangle$  of shadowgraph image differences. The inserts show schematically and experimentally the boundary layer and the patterns in the direction perpendicular to the gravity field. (a) The injection temporarily perturbs the contrast until the gaseous phase becomes stable and the contrast constant. (b) During this regime,  $\text{CO}_2$  spreads diffusively into brine, giving rise to an unstable growing boundary layer. (c) At  $t = t_c$ , the contrast rises when convective patterns suddenly appear. (d) After a short time, the first pattern reaches the maximum concentration  $C_{eq}$  of  $\text{CO}_2$  and further patterns appear. (e) The image variance reaches a maximum at  $t_m$ . (f) The plateau characterizes a stationary condition where the boundary layer thickness and the convective flux are constant. Here, the convective flow is essentially columnar. (g) The convective flow gradually mixes  $\text{CO}_2$  and brine, and patterns become less and less contrasted as they are dissipating diffusively. (h) Convection vanishes and the variance goes back to its initial level.

**Spatial scales.** From the analysis of the shadowgraph images we additionally obtain the time evolution of the plume density, defined as the number of plumes per surface area. The comparison between the plume density and the image contrast (Fig. 2) provides a further insight in the convective dissolution process. While the variance of image differences shows one maximum, the plume density presents two peaks. The first one takes place at the end of the phase of growth of convective patterns  $t_m$ . Advection is led by the maximum formation of plumes which are mostly within the stream tubes. Immediately after, isolated plumes and tubes merge, resulting in a small decrease of their density. The second peak occurs when the image difference contrast reaches a plateau. In the first phase of relaxation, the formation of new plumes comes at the expense of the split of stream tubes, as witnessed by the decrease in image difference variance. While some tubular patterns remain at this moment (Fig. 1 (f)), the plumes/columns density is at its maximum and the variance is almost constant. Finally, the plumes density decreases until it reaches zero after  $t_{sd}$ . Indeed, when the image contrast has reached its baseline value, there are still some

patterns in the bulk. The shut-down of convection actually takes place at  $t_{sd}$ , after which the remaining columns fade away by diffusion only. From the analysis of similar curves for different injection pressure we note that the maximum plume density increases with the Rayleigh number.

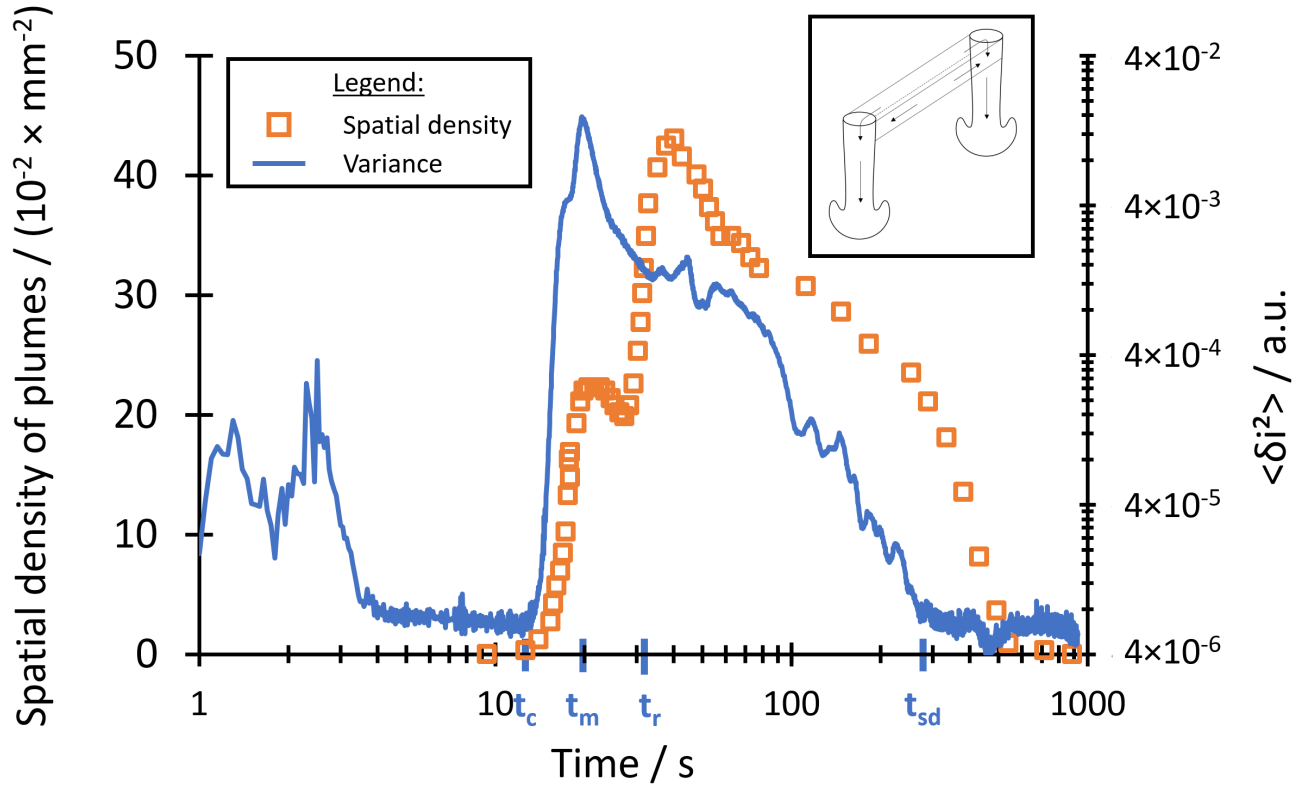


**Figure 2. Plume density as measured from the shadowgraph images** for an injection from 0.1 to 2.1 MPa (orange square symbols) plotted against optical contrast as in Fig. 1 (blue continuous line). After  $t_c$ , plumes appear within the tubes and the plume density rises. The latter reaches a first maximum around  $t_m$ , decreases and rapidly increases again after  $t_r$  due to the appearance of isolated plumes. Then, the plume density decreases and vanishes somewhat after  $t_{sd}$  corresponds to the end of the convective regime. (inset) Schematic representation of the plumes and their interconnection by horizontal stream tubes. The tubes are charging the plumes with brine with a high concentration of  $\text{CO}_2$  and eventually break into plumes.

**Scaling law based on boundary layer convection.** The stability of the fluid against convection is determined by the balance between the driving force of buoyancy and the dissipating effects of viscosity and mass diffusion, as expressed by the dimensionless global solutal Rayleigh number

$$Ra_s = \frac{g\Delta\rho h^3}{\eta D}, \quad (1)$$

where  $g$  is the gravity acceleration and  $h$  the overall liquid layer thickness. Swelling effects<sup>38</sup> are considered in the value of  $h$ .  $\Delta\rho$  is the density difference between the saturated liquid phase after and before  $\text{CO}_2$  injection.  $\eta$  and  $D$  are the dynamic viscosity and the Fick diffusion coefficient associated with the  $\text{CO}_2$ -brine mixture when macroscopic thermodynamic equilibrium is reached. For the present systems, the occurrence of convection is insensitive to the pressure dependence of  $D$  and  $\eta$ <sup>39</sup>. This is because the concentration of  $\text{CO}_2$  dissolved in brine or pure water remains small enough over the complete pressure range<sup>33</sup> such that  $D$  and  $\eta$  can be assumed constant<sup>40,41</sup>. Above a threshold critical value  $Ra_s^*$ , the system undergoes a symmetry-breaking mechanism leading to the appearance of a convective instability characterized by the formation of density patterns (Fig. 1).

A quantitative understanding of the scaling relation for the onset time, and in turn of the physical mechanism behind the instability can be achieved by considering the seminal model developed by Howard to describe the stability of a horizontal layer of fluid of infinite aspect ratio subjected to a temperature difference<sup>42</sup>. Howard investigated the onset of turbulence in a horizontal layer of fluid heated from below well above its critical Rayleigh number. Under these conditions, heat conduction

determines the rapid growth of a temperature boundary layer, which becomes unstable when it reaches a critical thickness. The instability determines the emission of plumes, which deplete the boundary layers, and the process iterates until the system reaches a stationary state where the boundary layer thickness is pinned at its critical value. Arguments very similar to those proposed by Howard have been successfully used to understand the onset of solutal boundary layer convection in suspensions of silica particles<sup>43–45</sup> and thermosensitive particles<sup>46,47</sup> triggered by the Soret effect, and during the dissolution of a solid into a liquid phase<sup>48</sup>.

In our experiments, a layer of brine with a thickness  $h$  is initially in equilibrium with a gaseous phase of CO<sub>2</sub> at atmospheric pressure. The imposition of a sudden jump of the pressure of CO<sub>2</sub> at the beginning of each experimental run determines an increase of the amount of CO<sub>2</sub> that can be dissolved into brine. As a result, CO<sub>2</sub> gradually diffuses into water and forms a mixed liquid boundary layer below the water-CO<sub>2</sub> interface. Since the density of mixtures of CO<sub>2</sub> and water is larger than that of water or brine itself, the boundary layer is intrinsically unstable against gravity<sup>28</sup>. Before convection sets-in, the time evolution of the diffusive growth of the boundary layer can be described analytically by solving the diffusion equation  $\partial c/\partial t = D(\partial c/\partial z)^2$ . The CO<sub>2</sub> phase overlying the layer of water can be modelled by adopting a boundary condition of constant concentration of CO<sub>2</sub> dissolved into water at the interface, while for the bottom of the water layer one can assume an impermeable boundary. For times much shorter than  $t_D$  (or for large sample thickness  $h$ ), the concentration profile can be approximated by the one obtained in a semi-infinite system, with the top boundary at concentration  $C_{eq}$  and the bulk of the fluid at  $C_0$ , yielding  $C(z) = C_0 + (C_{eq} - C_0)erfc[(h - z)/(\sqrt{4Dt})]$ <sup>49</sup>. Here,  $z$  is the vertical coordinate,  $z = 0$  represents the bottom of the sample, and the interface is located at  $z = h$ .

The systematic investigation of the injection of CO<sub>2</sub> at different pressure steps shows that the dimensionless time  $\tau_c = t_c/t_D$  needed for the onset of convection exhibits a power law behaviour as a function of the solutal Rayleigh number  $Ra_s$ , with exponent  $-(0.66 \pm 0.05)$ ; see Fig. 3. Interestingly, the time needed for the onset of convection is about two orders of magnitude smaller than the diffusive time  $t_D$  needed to achieve the diffusive dissolution of CO<sub>2</sub> even over a very thin layer, like in the case of our laboratory study.

Previous experimental and theoretical works came to the conclusion that the convective dissolution of CO<sub>2</sub> is slowed down by the presence of salt when the process occurs into brine, with respect to the times needed in pure water<sup>11–14</sup>. To elucidate this point we have determined experimentally the time needed for the onset of convection in pure water and in brine obtained by adding 1 or 3 mol/kg of NaCl to water. Although for the same pressure jump the time evolution of the contrast of shadowgraph images exhibits a delayed onset of convection, once the dimensionless solutal Rayleigh number is adopted for the parametrization of the results, we find that data points for pure water and brine collapse on the same master curve expressed by equation 4 (Fig. 3). Therefore, the slowing down of the onset of convection in brine is only associated with the difference in the solutal Rayleigh number. This is valid for both, the Rayleigh-Taylor and Rayleigh-Darcy regimes, i.e. in free or in porous media.

To model the onset of convection we assume that the concentration profile in the liquid layer can be divided into two regions: a boundary layer region at the top, where the concentration varies linearly, and a bulk region at the bottom, where the concentration is essentially uniform. The thickness  $d$  of the boundary layer, estimated as the vertical extension of the linear region, changes in time diffusively as  $d(t) = \sqrt{\pi Dt}$ , and in dimensionless form

$$\delta(\tau) = \sqrt{\tau}. \quad (2)$$

During the initial diffusive growth, the boundary layer is horizontally uniform (except for tiny non-equilibrium concentration fluctuations<sup>50</sup>) and the contrast of shadowgraph images does not change significantly. When the boundary layer reaches a critical thickness  $\delta^*$ , it becomes unstable and convection sets-in at time  $\tau^* = \tau_c$ . Thereafter, plumes start to cross the cell in the vertical direction. Following Howard, the stability of the boundary layer can be characterized by introducing a local solutal Rayleigh number<sup>42</sup>,  $Ra_{\delta,s}$ , defined across the thickness  $\delta$  of the boundary layer. Introducing the dimensionless critical boundary layer thickness  $\delta^* = d^*/h$ , when the local Rayleigh number exceeds the critical value

$$Ra_{\delta,s}^* = Ra_s \delta^{*3}. \quad (3)$$

convection sets-in in the form of down-welling plumes.

In the case of a biphasic system like gaseous or super-critical CO<sub>2</sub> over liquid water with free boundary conditions<sup>47</sup>,  $Ra_{\delta}^* = 27\pi^4/4 = 657.5$ . Combining Eqns. 2 and 3 we obtain the scaling relation for the dimensionless critical time needed for the onset of the instability:

$$\tau^* = \left( \frac{Ra_s}{Ra_{\delta,s}^*} \right)^{-\frac{2}{3}}, \quad (4)$$

which is fully compatible with the experimental results for the onset time shown in Fig. 3.

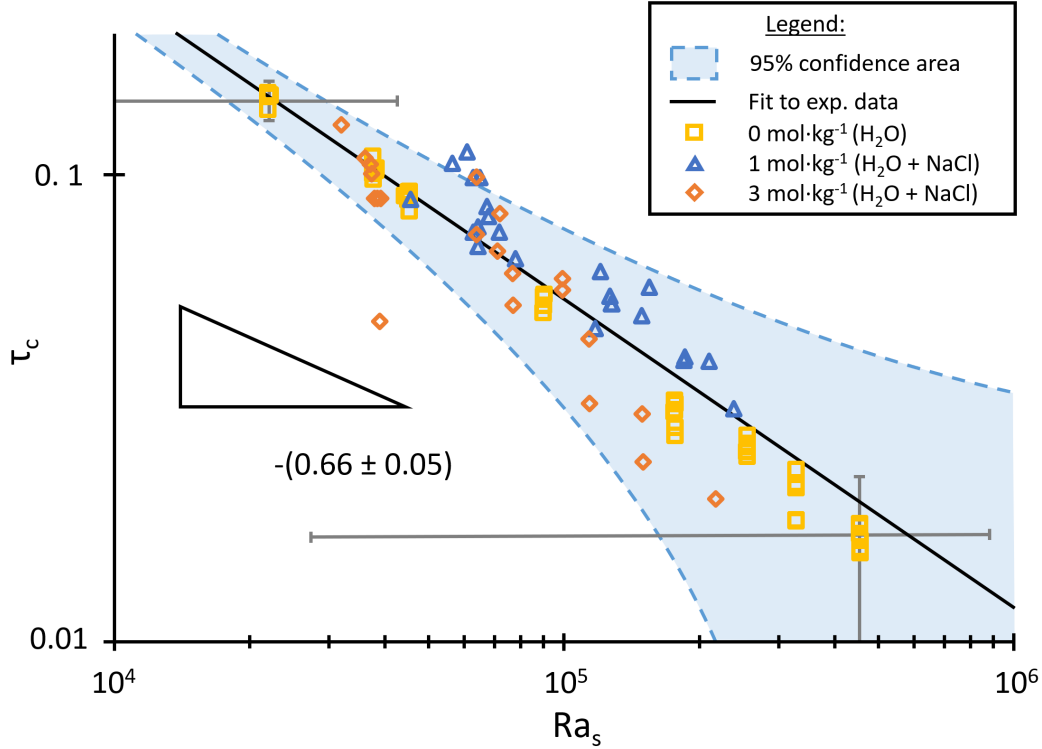


**Figure 3. Log-log plot of the dimensionless onset time  $\tau_c$  as a function of the solutal Rayleigh number.** The experimental data are plotted with squares (pure water), triangles (brine at  $1 \text{ mol}\cdot\text{kg}^{-1}$  of NaCl) and diamonds (brine at  $3 \text{ mol}\cdot\text{kg}^{-1}$  of NaCl). The continuous black line corresponds to the fit to experimental data with a power law:  $\tau_c = 104 \cdot Ra_s^{-0.66}$ . The blue shaded area corresponds to the 95% confidence level of the fit to the experimental data. Error bars illustrate the expanded uncertainties ( $k = 2$ ) of experimental data. Large error bars in  $Ra_s$  are mainly associated with the large experimental uncertainty of the liquid layer thickness. The expanded experimental uncertainties of  $\tau_c$  and  $Ra_s$  have been derived using the uncertainties on  $t_c$  and  $h$  as well as the uncertainties on the other thermophysical properties taken from the literature. The standard deviation between repeated measurements is much smaller than the corresponding experimental uncertainty.

## Discussion

After the onset of the instability and in the presence of a stable driving concentration difference  $\Delta C = C_{\text{eq}} - C_0$ , the system reaches a stationary convective state where the transfer of mass occurs diffusively in the boundary layer at the critical thickness  $d^*$ , while it occurs convectively in the bulk of the sample. Mass conservation imposes that the diffusive flux  $j_d = -\rho D \Delta C / d^*$  inside the boundary layer must be equal to the convective flux outside of it. Introducing the solutal Nusselt number as the ratio of the overall mass flow and the diffusive mass flux  $j_h = -\rho D \Delta C / h$  across the entire thickness of the sample yields:

$$Nu_s = \frac{j_d}{j_h} = \frac{h}{d^*} = \frac{1}{\delta^*}. \quad (5)$$

Combining Eqns. 3-5 yields the scaling relation:

$$Nu_s = \left( \frac{Ra_s}{Ra_\delta^*} \right)^{\frac{1}{3}}. \quad (6)$$

Similar experimental results and theoretical modelling were found for the turbulent convective transfer of heat in a single component fluid at high thermal Rayleigh  $Ra_T$  and Prandtl numbers<sup>29-32</sup>, a problem formally equivalent to the one that we are discussing here notwithstanding the completely different physical origin of the density unbalance driving the convective process. They found a scaling relation  $Nu_T \propto Ra_T^{1/3}$  fully equivalent to Eqn. 6, where  $Nu_T$  is the thermal Nusselt number. The analogy with heat convection at large thermal Rayleigh numbers has been recently exploited to perform fully 3-dimensional simulations of Rayleigh-Darcy convection in a porous medium<sup>51</sup>. These simulations showed that the confinement determined

by the porous medium strongly affects the scaling relation for  $Nu_T$  in the large  $Ra_T$  regime, which becomes a proportionality relation  $Nu_T \propto Ra_T$ , in agreement with theoretical predictions<sup>10</sup>.

An important consequence of Eqn. 5 is that the convective mass flux at steady state can be inferred from the onset time  $\tau_c$  needed for the onset of convection. In fact, the onset time  $\tau_c$  allows to determine the critical thickness  $\delta^*$  of the boundary layer (Eqn. 2), and in turn the solutal Nusselt number. Under the range of solutal Rayleigh numbers explored by us the power law exponent is  $(0.38 \pm 0.03)$  (Fig. 4), compatible with the exponent 1/3 of Eq. 6 and with the experimental exponent of 0.31 reported for turbulent heat convection over a wide range of Rayleigh number<sup>30</sup>.

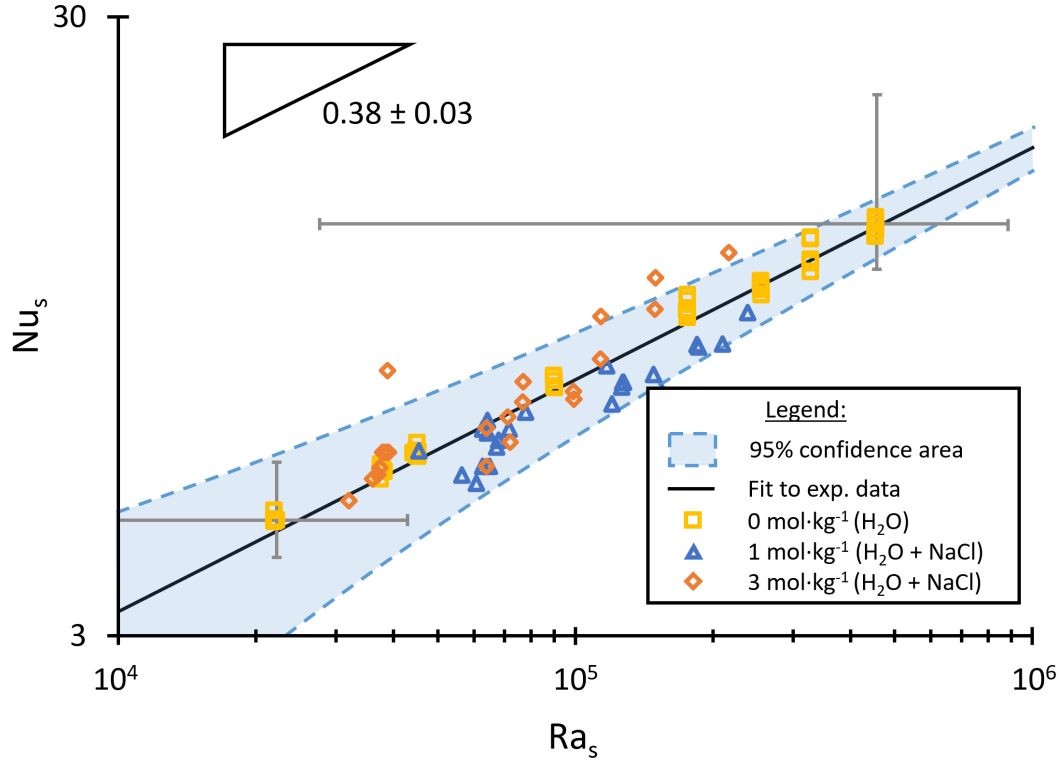


**Figure 4. Solutal Nusselt number against solutal Rayleigh number.** The experimental data are plotted with squares (water), triangles (brine at  $1 \text{ mol}\cdot\text{kg}^{-1}$  of NaCl) and diamonds (brine at  $3 \text{ mol}\cdot\text{kg}^{-1}$  of NaCl). The continuous black line correspond to the the fitting with a power law. The blue shaded area corresponds to the 95% confidence level of the fit to the experimental data.

The availability of a model of the convective dissolution process by means of dimensionless equations allows to project this result at the geological length scales of interest for the convective dissolution of  $\text{CO}_2$  into deep saline aquifers. For example, by assuming a thickness  $h = 100 \text{ m}$  for the aquifer, Eqn. 5 lets us estimate the solutal Nusselt number of the order of  $10^4$ .

Going back to dimensioned variables, from Eqns. 1 and 4 we obtain the remarkable result that the dimensioned onset time  $t_c$  needed for the onset of convection and the convective flux  $j_d$  at steady state do not depend on the size  $h$  of the system, and represent scale-free features for the convective dissolution of  $\text{CO}_2$ :

$$t_c = \frac{1}{\pi D} \left( \frac{\rho \nu D}{g \Delta \rho} Ra_\delta^* \right)^{\frac{2}{3}}, \quad (7)$$

$$j_d = \frac{D}{\beta} \left( \frac{g}{\rho \nu D} \frac{1}{Ra_\delta^*} \right)^{\frac{1}{3}} \Delta \rho^{\frac{4}{3}} \quad (8)$$

where  $\beta = (1/\rho)(\partial\rho/\partial c)$  is the solutal expansion coefficient.

The physical reason behind the absence of a dependence of  $t_c$  and  $j_d$  from the typical length scale  $h$  of the system is that the boundary layer instability occurs very rapidly, when the boundary layer thickness is still much smaller than that of the

laboratory liquid sample or of the aquifer. For this reason, the presence of an impermeable boundary at a depth  $h$  below the CO<sub>2</sub>-water interface is still not felt when the boundary layer becomes unstable, and the only relevant length-scale is the critical boundary layer thickness. This feature is akin to thermal turbulence in a layer of fluid, where it is well known that the heat transferred for a given temperature difference is independent of the spacing between the thermalizing plates<sup>52</sup>.

The scaling laws presented in this work are valid only in free media. As stated above, in the presence of a porous medium, or in Hele-Shaw configurations, the Nusselt number becomes proportional to a Rayleigh-Darcy number and thus it increases much more rapidly. Thus, the convective dissolution of CO<sub>2</sub> in the brine should be much more efficient than diffusion only.

This approach has been used to perform fully 3-dimensional simulations of heat convection at large Rayleigh-Darcy numbers and at infinite Prandtl number, which showed that the approach proposed by Howard can be adopted successfully also in the presence of a porous medium, leading to scaling relations similar to Eqns. 3-6, but with different power law exponents<sup>51</sup>.

Experiments in realistic porous media will be needed to confirm the latter theoretical predictions and understand if the boundary layer mechanism is still valid to describe the phenomenon of convective dissolution. The existence of scaling laws describing the system behaviour allows up-scaling our results to the basin scale.

## Methods

### Materials and sample preparation

Distilled water of Millipore grade and sodium chloride (NaCl), purchased from Fischer-Scientific, are degassed separately with the help of a two-stage oil-sealed rotary vane vacuum pump for about 30 minutes. The purity by mass of NaCl specified by the supplier is 99.5 %. All brine mixtures were prepared gravimetrically with the help of a balance from Ohaus (Scout\*) with a specified precision of 1 mg, where an absolute expanded measurement uncertainty of 0.2% was estimated. As solute, CO<sub>2</sub> from Linde with a purity better than 99.995 vol.% was employed.

Brine is injected in the sample cell using a syringe pump with a flow rate of 1 mL·min<sup>-1</sup>. The sample cell was evacuated and, then, filled with 0.1 MPa of CO<sub>2</sub> beforehand for limiting the influence of residual gases contained in the atmosphere. The volume of brine injected inside the sample cell is controlled in order to fix the initial liquid layer thickness to 2 mm.

### High-pressure convection cell

The experimental cell consists of a polytetrafluoroethylene (PTFE) ring inserted inside a stainless-steel block that is vertically confined between 2 sapphire windows. Since PTFE is highly hydrophobic, a thin layer of a hydrophilic polymer was added to the PTFE ring interior in order to have an almost flat gas-liquid interface. Such device can host a cylindrical sample of 5 mm height and 20 mm diameter. The cell hosts one inlet close to the upper window to inject the gas and one inlet close to the bottom window to inject the brine. The cell is thermally controlled with two Peltier elements, a thermal bath, and three insulation layers, to work at a constant temperature of 308.2 K. The injection of CO<sub>2</sub> is performed by two ISCO DM500 pumps that keep the pressure constant during the time of the experiment. The inclination of the horizontal side of the cell is monitored with a calibrated inclinometer from Digi-Pas (DWL5000XY) and tuned to better than 9 mrad.

### Shadowgraph setup and image processing

The optical technique is that of a shadowgraph<sup>34-37</sup> comprising a super-luminous diode from Superlum with a wavelength of (675±13) nm, coupled to a single mode optical fiber as a light source. The diverging beam out of the fiber is collimated by using an achromatic doublet lens of focal length 250 mm positioned at the focal distance from the lens. A scientific complementary metal-oxide-semiconductor camera (Hamamatsu, ORCA-Flash4.0 V3) with a resolution of 2048x2048 pixels of 6.5 μm is placed at a distance of about 100 mm from the sample plane. The complete setup is mounted on a vibration-damped optical table. A drawing of the optical arrangement can be found in Ref.<sup>53</sup>.

The image processing consists in normalizing each image by its average intensity value and, then, subtracting them by a reference image. The reference image, or "background", corresponds to the average intensity map between 5 normalized images acquired before the injection of CO<sub>2</sub>. Thereafter, we computed the variance  $\langle \delta i^2 \rangle$  of each image difference.

### Solutal Rayleigh number calculations

**Liquid layer thickness.** Solutal Rayleigh numbers were estimated from Eqn. 1 using the experimental liquid layer thickness  $h = 2$  mm, corrected by the swelling factor<sup>38</sup> at a given pressure, and further thermophysical property data from the literature or that have been calculated. The swelling factor is assumed to be independent of the salinity of brine. Corresponding  $Ra_s$  data are determined at macroscopic thermodynamic equilibrium when the dissolution process is complete.

**Fick diffusion coefficient,** solute self-diffusivity, and solute tracer diffusion coefficient are equal in the infinite dilution regime<sup>40</sup>. For that reason, diffusivity data collected from the literature are at different pressures along the vapor-liquid equilibrium. The Fick diffusion coefficient associated with pure water containing dissolved CO<sub>2</sub> used in the calculation of  $Ra_s$

at a temperature of 308.15 K is of  $2.76 \times 10^{-9} \text{ m}^2 \cdot \text{s}^{-1}$ . This value was obtained from the fit to its temperature dependence<sup>39</sup> between 298.15 and 423.15 K using an Arrhenius-type correlation<sup>54</sup>. The average absolute relative deviation (AARD) and the bias between experimental and modeled diffusivities are 2.37 % and -0.07 %, respectively. Experimental data from other references, e.g., Refs.<sup>55–57</sup>, were not considered. This is because the results are not consistent with the model<sup>58</sup> for NaCl/water mixtures, as well as because, in most cases, uncertainties were not given. The complete dataset<sup>39,55–57</sup> collected in the literature shows a double standard deviation of 68.05 % on  $D$  at  $T=308.15$  K. The Fick diffusion coefficient of CO<sub>2</sub> and NaCl/water mixtures were determined using a Stokes-Einstein-like model<sup>58</sup>, wherein the hydrodynamic radius is temperature-dependent and the dynamic viscosities are taken at atmospheric pressure from Kestin et al.<sup>59</sup>. For comparison purposes, the modeled diffusivities were compared to experimental ones at  $T = 298.15$  K<sup>57,58</sup>. The AARD and bias are 7.92 % and 6.03 %, where the largest deviations are associated with the old experimental data from Himmelblau<sup>57</sup>. At  $T = 308.15$  K, we found  $D = (2.59$  and  $2.06) \times 10^{-9} \text{ m}^2 \cdot \text{s}^{-1}$  for NaCl molalities of 1 and 3 mol·kg<sup>-1</sup>. The same correlation provides  $D = 2.79 \times 10^{-9} \text{ m}^2 \cdot \text{s}^{-1}$  for pure water at the same temperature, which is fully compatible with the one obtained from the Arrhenius-type correlation.

**Dynamic viscosity**,  $\eta$  of brine mixtures for the three molalities of salt, i.e. (0, 1, and 3) mol·kg<sup>-1</sup>, at the different pressures were derived from the model proposed by Kestin et al.<sup>59</sup>. They estimated that the correlation has an overall accuracy of  $\pm 0.5\%$ . The influence of the amount of CO<sub>2</sub> dissolved in brine was neglected. This assumption is supported by the work of Fleury et al.<sup>60</sup> who showed that a change in the molar fraction of CO<sub>2</sub> from 0 to 2 mol.% induces a variation in  $\eta$  of less than 8 % for NaCl molalities between (0.32 and 2.92) mol·kg<sup>-1</sup> and temperatures between (308.15 and 373.15) K. The larger is the temperature, the smaller the variation in  $\eta$ . 2 mol.% represents the largest amount of CO<sub>2</sub> dissolved in brine in our experiments<sup>61</sup>. Furthermore, deviations in  $\eta$  are smaller than the typical deviations observable between different correlations that can be found in the literature<sup>60,62–64</sup>. Including the variation of  $\eta$  as a function of the concentration of CO<sub>2</sub>, which needs to be modeled, will give rise to larger uncertainties in our calculations of  $Ra_s$ .

**Densities** were calculated using PhreeqC v3.7.2a<sup>65</sup> embedding the Peng-Robinson equation of state<sup>66</sup>. Calculated densities were compared to experimental densities<sup>67</sup> on CO<sub>2</sub>-saturated brine mixtures for NaCl molalities between (0 and 5) mol·kg<sup>-1</sup>. The AARD and bias between the experimental data and the modeled densities are 0.11 % and -0.07 %, respectively.

## References

1. Manabe, S. & Wetherald, R. T. Thermal equilibrium of the atmosphere with a given distribution of relative humidity. *J. Atmospheric Sci.* **24**, 241–259 (1967).
2. Edenhofer, O. *et al.* IPCC: Climate change 2014: Mitigation of climate change. Contribution of working group III to the fifth assessment report of the intergovernmental panel on climate change (2014).
3. Gates, B. *How to Avoid a Climate Disaster: The Solutions We Have and the Breakthroughs We Need* (Random House Large Print, USA, 2021).
4. Haas, T., Krause, R., Weber, R., Demler, M. & Schmid, G. Technical photosynthesis involving CO<sub>2</sub> electrolysis and fermentation. *Nat. Catal.* **1**, 32–39 (2018).
5. Jiao, F. *et al.* Selective conversion of syngas to light olefins. *Science* **351**, 1065–1068 (2016).
6. Michael, K. *et al.* Geological storage of CO<sub>2</sub> in saline aquifers — a review of the experience from existing storage operations. *Int. J. Greenh. Gas Control.* **4**, 659–667 (2010).
7. Rochelle, G. T. Amine scrubbing for CO<sub>2</sub> capture. *Science* **325**, 1652–1654 (2009).
8. Bickle, M. J. Geological carbon storage. *Nat. Geosci.* **2**, 815–818 (2009).
9. Ennis-King, J. P. & Paterson, L. Role of convective mixing in the long-term storage of carbon dioxide in deep saline formations. *SPE J.* **10**, 349–356 (2005).
10. Huppert, H. E. & Neufeld, J. A. The fluid mechanics of carbon dioxide sequestration. *Annu. Rev. Fluid Mech.* **46**, 255–272 (2014).
11. Tang, Y. *et al.* Experimental study on the density-driven carbon dioxide convective diffusion in formation water at reservoir conditions. *ACS Omega* **4**, 11082–11092 (2019).
12. Khosrokhavar, R., Elsinga, G., Farajzadeh, R. & Bruining, H. Visualization and investigation of natural convection flow of CO<sub>2</sub> in aqueous and oleic systems. *J. Petroleum Sci. Eng.* **122**, 230–239 (2014).
13. Loodts, V., Rongy, L. & De Wit, A. Impact of pressure, salt concentration, and temperature on the convective dissolution of carbon dioxide in aqueous solutions. *Chaos: An Interdiscip. J. Nonlinear Sci.* **24**, 043120 (2014).
14. Thomas, C., Dehaeck, S. & De Wit, A. Convective dissolution of CO<sub>2</sub> in water and salt solutions. *Int. J. Greenh. Gas Control.* **72**, 105–116 (2018).

15. Ambrose, W. A. *et al.* Geologic factors controlling CO<sub>2</sub> storage capacity and permanence: case studies based on experience with heterogeneity in oil and gas reservoirs applied to CO<sub>2</sub> storage. *Environ. Geol.* **54**, 1619–1633 (2008).
16. Amarasinghe, W., Fjelde, I., Rydland, J.-Å. & Guo, Y. Effects of permeability on CO<sub>2</sub> dissolution and convection at reservoir temperature and pressure conditions: A visualization study. *Int. J. Greenh. Gas Control.* **99**, 103082 (2020).
17. Amarasinghe, W. S., Fjelde, I. & Flaata, A. M. N. Visual investigation of CO<sub>2</sub> dissolution and convection in heterogeneous porous media at reservoir temperature and pressure conditions. *Greenh. Gases: Sci. Technol.* **11**, 342–359 (2021).
18. Mojtaba, S., Behzad, R., Rasoul, N. M. & Mohammad, R. Experimental study of density-driven convection effects on CO<sub>2</sub> dissolution rate in formation water for geological storage. *J. Nat. Gas Sci. Eng.* **21**, 600–607 (2014).
19. Vosper, H., Kirk, K., Rochelle, C., Noy, D. & Chadwick, A. Does numerical modelling of the onset of dissolution-convection reliably reproduce this key stabilization process in CO<sub>2</sub> storage? *Energy Procedia* **63**, 5341–5348 (2014).
20. Outeda, R., Hasi, C. E., D'Onofrio, A. & Zalts, A. Experimental study of linear and nonlinear regimes of density-driven instabilities induced by CO<sub>2</sub> dissolution in water. *Chaos: An Interdiscip. J. Nonlinear Sci.* **24**, 013135 (2014).
21. Faisal, T. F., Chevalier, S., Bernabe, Y., Juanes, R. & Sassi, M. Quantitative and qualitative study of density driven CO<sub>2</sub> mass transfer in a vertical hele-shaw cell. *Int. J. Heat Mass Transf.* **81**, 901–914 (2015).
22. Vreme, A. *et al.* Gravitational instability due to the dissolution of carbon dioxide in a Hele-Shaw cell. *Phys. Rev. Fluids* **1** (2016).
23. Lu, G. *et al.* Study of density driven convection in a Hele-Shaw cell with application to the carbon sequestration in aquifers. *Energy Procedia* **114**, 4303–4312 (2017).
24. Taheri, A., Torsæter, O., Lindeberg, E., Hadia, N. J. & Wessel-Berg, D. Qualitative and quantitative experimental study of convective mixing process during storage of CO<sub>2</sub> in heterogeneous saline aquifers. *Int. J. Greenh. Gas Control.* **71**, 212–226 (2018).
25. Teng, Y., Wang, P., Jiang, L., Liu, Y. & Wei, Y. New spectrophotometric method for quantitative characterization of density-driven convective instability. *Polymers* **13**, 661 (2021).
26. De Paoli, M., Alipour, M. & Soldati, A. How non-Darcy effects influence scaling laws in Hele-Shaw convection experiments. *J. Fluid Mech.* **892**, 1–15 (2020).
27. Soltanian, M. R., Amooie, M. A., Dai, Z., Cole, D. & Moortgat, J. Critical dynamics of gravito-convective mixing in geological carbon sequestration. *Sci. Reports* **6**, 35921 (2016).
28. Lindeberg, E. & Wessel-Berg, D. Vertical convection in an aquifer column under a gas cap of CO<sub>2</sub>. *Energy Convers. Manag.* **38**, S229–S234 (1997).
29. Siggia, E. D. High Rayleigh number convection. *Annu. Rev. Fluid Mech.* **26**, 137–168 (1994).
30. Niemela, J. J., Skrbek, L., Sreenivasan, K. R. & Donnelly, R. J. Turbulent convection at very high Rayleigh numbers. *Nature* **404**, 837–840 (2000).
31. Grossmann, S. & Lohse, D. Thermal convection for large Prandtl numbers. *Phys. Rev. Lett.* **86**, 3316–3319 (2001).
32. Fleischer, A. S. & Goldstein, R. J. High-Rayleigh-number convection of pressurized gases in a horizontal enclosure. *J. Fluid Mech.* **469**, 1–12 (2002).
33. Spycher, N. & K., P. CO<sub>2</sub>-H<sub>2</sub>O mixtures in the geological sequestration of CO<sub>2</sub>. i. assessment and calculation of mutual solubilities from 12 to 100°C and up to 600 bar. *Geochimica Cosmochimica Acta* **67**, 3015–3031 (2003).
34. Croccolo, F. & Brogioli, D. Quantitative Fourier analysis of schlieren masks: the transition from shadowgraph to schlieren. *App. Opt.* **50**, 3419 (2011).
35. Wu, W., Jander, J. H., Rausch, M. H., Fröba, A. P. & Giraudet, C. Simultaneous determination of multiple transport properties over a wide range of temperatures and pressures from the analysis of non-equilibrium fluctuations by the shadowgraph method. *J. Chem. Phys.* **153**, 144201 (2020).
36. Croccolo, F., Bataller, H. & Scheffold, F. A light scattering study of non equilibrium fluctuations in liquid mixtures to measure the Soret and mass diffusion coefficient. *J. Chem. Phys.* **137**, 234202 (2012).
37. Croccolo, F., Scheffold, F. & Vailati, A. Effect of a marginal inclination on pattern formation in a binary liquid mixture under thermal stress. *Phys. Rev. Lett.* **111**, 014502 (2013).
38. Li, X., Song, Y., Wu, B., Liu, Y. & Jiang, L. Determination of swelling effect in CO<sub>2</sub>-brine systems using microfocus X-ray CT. *Energy Procedia* **142**, 3344–3349 (2017).

39. Cadogan, S. P., Maitland, G. C. & Trusler, J. P. M. Diffusion coefficients of CO<sub>2</sub> and N<sub>2</sub> in water at temperatures between 298.15 K and 423.15 K at pressures up to 45 MPa. *J. Chem. Eng. Data* **59**, 519–525 (2014).
40. Wu, W. *et al.* Diffusivities in 1-alcohols containing dissolved H<sub>2</sub>, He, N<sub>2</sub>, CO, or CO<sub>2</sub> close to infinite dilution. *J. Phys. Chem. B* **123**, 8777–8790 (2019).
41. Wu, W. *et al.* Mutual and thermal diffusivities as well as fluid-phase equilibria of mixtures of 1-hexanol and carbon dioxide. *J. Phys. Chem. B* **124**, 2482–2494 (2020).
42. Görtler, H. *Applied Mechanics : Proceedings of the Eleventh International Congress of Applied Mechanics Munich (Germany) 1964* (Springer Berlin Heidelberg Imprint Springer, Berlin, Heidelberg, 1966).
43. Mazzoni, S., Cerbino, R., Brogioli, D., Vailati, A. & Giglio, M. Transient oscillations in Soret-driven convection in a colloidal suspension. *The Eur. Phys. J. E* **15**, 305–309 (2004).
44. Cerbino, R., Mazzoni, S., Vailati, A. & Giglio, M. Scaling behavior for the onset of convection in a colloidal suspension. *Phys. Rev. Lett.* **94**, 064501 (2005).
45. Giavazzi, F. & Vailati, A. Scaling of the spatial power spectrum of excitations at the onset of solutal convection in a nanofluid far from equilibrium. *Phys. Rev. E* **80** (2009).
46. Winkel, F. *et al.* Thermal convection in a thermosensitive colloidal suspension. *New J. Phys.* **12**, 053003 (2010).
47. Messlinger, S., Schöpf, W. & Rehberg, I. Transient diffusive boundary layers at high Rayleigh numbers in simple and double diffusive fluids: Latency time scaling for the convection onset. *Int. J. Heat Mass Transf.* **62**, 336–349 (2013).
48. Philippi, J., Berhanu, M., Derr, J. & du Pont, S. Solutal convection induced by dissolution. *Phys. Rev. Fluids* **4**, 103801 (2019).
49. Crank, J. *The mathematics of diffusion* (Oxford University Press, Oxford UK, 1975).
50. Croccolo, F., Ortiz de Zarate, J. & Sengers, J. Non-local fluctuation phenomena in liquids. *Eur. Phys. J. E* **39**, 125 (2016).
51. Pirozzoli, S., Paoli, M. D., Zonta, F. & Soldati, A. Towards the ultimate regime in Rayleigh–Darcy convection. *J. Fluid Mech.* **911**, R4 (2021).
52. Elder, J. W. The unstable thermal interface. *J. Fluid Mech.* **32**, 69–96 (1968).
53. Giraudet, C. *et al.* Confinement effect on the dynamics of non-equilibrium concentration fluctuations far from the onset of convection. *Eur. Phys. J. E* **39**, 1–13 (2016).
54. Giraudet, C. *et al.* Thermal, mutual, and self-diffusivities of binary liquid mixtures consisting of gases dissolved in *n*-alkanes at infinite dilution. *J. Phys. Chem. B* **122**, 31633175 (2018).
55. Frank, M. J., Kuipers, J. A. & van Swaaij, W. P. Diffusion coefficients and viscosities of CO<sub>2</sub> + H<sub>2</sub>O, CO<sub>2</sub> + CH<sub>3</sub>OH, NH<sub>3</sub> + H<sub>2</sub>O, and NH<sub>3</sub> + CH<sub>3</sub>OH liquid mixtures. *J. Chem. Eng. Data* **41**, 297–302 (1996).
56. Unver, A. A. & Himmelblau, D. M. Diffusion coefficients of CO<sub>2</sub>, C<sub>2</sub>H<sub>4</sub>, C<sub>3</sub>H<sub>6</sub> and C<sub>4</sub>H<sub>8</sub> in water from 6° to 65°C. *J. Chem. Eng. Data* **9**, 428–431 (1964).
57. Himmelblau, D. M. Diffusion of dissolved gases in liquids. *Chem. reviews* **64**, 527–550 (1964).
58. Cadogan, S. P., Hallett, J. P., Maitland, G. C. & Trusler, J. P. M. Diffusion coefficients of carbon dioxide in brines measured using <sup>13</sup>C pulsed-field gradient nuclear magnetic resonance. *J. Chem. Eng. Data* **60**, 181–184 (2015).
59. Kestin, J., Khalifa, E. H. & Correia, R. J. Tables of the dynamic and kinematic viscosity of aqueous NaCl solutions in the temperature range 20–150°C and the pressure range 0.1–35 MPa. *J. Phys. Chem. Ref. Data* **10**, 71–88 (1981).
60. Fleury, M. & Deschamps, H. Electrical conductivity and viscosity of aqueous NaCl solutions with dissolved CO<sub>2</sub>. *J. Chem. Eng. Data* **53**, 2505–2509 (2008).
61. Diamond, L. W. & Akinfiev, N. N. Solubility of CO<sub>2</sub> in water from -1.5 to 100°C and from 0.1 to 100 MPa: Evaluation of literature data and thermodynamic modelling. *Fluid Phase Equilibria* **208**, 265–290 (2003).
62. Kumagai, A. & Yokoyama, C. Viscosities of aqueous NaCl solutions containing CO<sub>2</sub> at high pressures. *J. Chem. Eng. Data* **44**, 227–229 (1999).
63. Kumagai, A. & Yokoyama, C. Viscosity of aqueous NaCl solutions with dissolved CO<sub>2</sub> at (30 to 60)°C and (10 to 20) mpa. *J. Chem. Eng. Data* **49**, 1328–1332 (2004).
64. Islam, A. W. & Carlson, E. S. Viscosity models and effects of dissolved CO<sub>2</sub>. *Energy Fuels* **26**, 5330–5336 (2012).

65. Parkhurst, D. L. & Appelo, C. A. Description of input and examples for phreeqc version 3: a computer program for speciation, batch-reaction, onedimensional transport, and inverse geochemical calculations. Technical report. U.S. Geological Survey (2013).
66. Peng, D.-Y. & Robinson, D. B. A new two-constant equation of state. *Ind. Eng. Chem. Fundamentals* **15**, 59–64 (1976).
67. Yan, W., Huang, S. & Stenby, E. H. Measurement and modeling of CO<sub>2</sub> solubility in NaCl brine and CO<sub>2</sub>-saturated NaCl brine density. *Int. J. Greenh. Gas Control*. **5**, 1460–1477 (2011).

## **Acknowledgements**

This research was carried under the framework of the E2S UPPA Hub Newpores and Industrial Chair CO2ES supported by the Investissements d’Avenir French programme managed by ANR (ANR16IDEX0002). Further support from CNES is gratefully acknowledged.

## **Author contributions statement**

F.C. conceived the project. F.C., C.G. and P.F. conceived the experiments. P.F. and A.N. conducted the experiments. F.C., C.G., P.F. and A.V. analyzed the results and wrote the manuscript. H.B. reviewed the manuscript.

## **Additional information**

The authors declare no competing financial interest. The corresponding author is submitting the manuscript on behalf of all listed authors.